JOURNAL OF SYNCHROTRON RADIATION
ISSN 1600-5775

Synchrotron radiation micro-tomography for high-resolution neurovascular network morphology investigation

Yong Cao,[a,b,c]‡ Mengqi Zhang,[d]‡ Hui Ding,[d] Zhuohui Chen,[d] Bin Tang,[d] Tianding Wu,[a,b,c] Bo Xiao,[d] Chunyue Duan,[a,b,c] Shuangfei Ni,[a,b,c] Liyuan Jiang,[a,b,c] Zixiang Luo,[a,b,c] Chengjun Li,[a,b,c] Jinyun Zhao,[a,b,c] Shenghui Liao,[e] Xianzhen Yin,[f] Yalan Fu,[g] Tiqiao Xiao,[g] Hongbin Lu[b,c,h]* and Jianzhong Hu[a,b,c]*

[a]Department of Spine Surgery, Xiangya Hospital, Central South University, Changsha 410008, People's Republic of China, [b]Key Laboratory of Organ Injury, Aging and Regenerative Medicine of Hunan Province, Changsha, Hunan 410008, People's Republic of China, [c]Xiangya Hospital-International Chinese Musculoskeletal Research Society Sports Medicine Research Center, Changsha, Hunan 410008, People's Republic of China, [d]Department of Neurology, Xiangya Hospital, Central South University, Changsha 410008, People's Republic of China, [e]School of Information Science and Engineering, Central South University, Changsha 410008, People's Republic of China, [f]Center for Drug Delivery System, Shanghai Institute of Materia Medica, Chinese Academy of Sciences, Shanghai 20203, People's Republic of China, [g]Shanghai Synchrotron Radiation Facility/Zhangjiang Lab, Shanghai Advanced Research Institute, Chinese Academy of Sciences, Shanghai 21204, People's Republic of China, and [h]Department of Sport Medicine, Xiangya Hospital, Central South University, Changsha 410008, People's Republic of China. *Correspondence e-mail: hongbinlu@hotmail.com, jianzhonghu@hotmail.com

Received 8 October 2018
Accepted 27 February 2019

Edited by I. Lindau, SLAC/Stanford University, USA

‡ These authors contributed equally to this work.

Keywords: high-resolution; imaging; neurovascular network; 3D.

There has been increasing interest in using high-resolution micro-tomography to investigate the morphology of neurovascular networks in the central nervous system, which remain difficult to characterize due to their microscopic size as well as their delicate and complex 3D structure. Synchrotron radiation X-ray imaging, which has emerged as a cutting-edge imaging technology with a high spatial resolution, provides a novel platform for the non-destructive imaging of microvasculature networks at a sub-micrometre scale. When coupled with computed tomography, this technique allows the characterization of the 3D morphology of vasculature. The current review focuses on recent progress in developing synchrotron radiation methodology and its application in probing neurovascular networks, especially the pathological changes associated with vascular abnormalities in various model systems. Furthermore, this tool represents a powerful imaging modality that improves our understanding of the complex biological interactions between vascular function and neuronal activity in both physiological and pathological states.

1. Introduction

Vascular diseases of the central nervous system, including aneurysms, atherosclerotic and arteriovenous malformations (AVMs), represent huge health and economic burdens and can lead to serious neurological problems or even death (Mouchtouris *et al.*, 2015; Krings, 2010). The early stages of these diseases are closely associated with small vessel lesions that are reflected by injury to the microvasculature. The microvasculature network in the central nervous system is arguably the most delicate 3D structure among all biological organs (Marín-Padilla, 2012; Martirosyan *et al.*, 2011). However, there are limitations to our understanding of the changes in the 3D morphology of small vessel lesions at the resolution of current imaging techniques. The detection and precise description of small vessel lesions in 3D space at a very early stage might also improve disease diagnosis and prognosis.

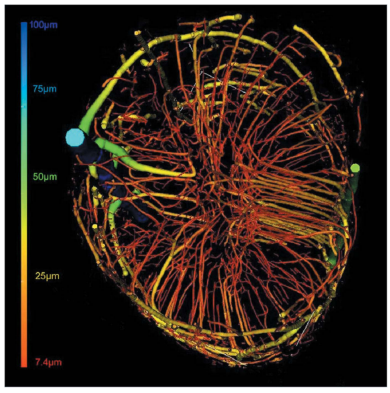

Current work aimed at improving the diagnosis of vascular diseases in clinical practice involves digital subtraction angiography (DSA), magnetic resonance angiography (MRA) and computed tomography angiography (CTA). However, all of these techniques lack sufficient imaging resolution to detect vasculature on a micrometre or sub-micrometre level (Mori *et al.*, 1994, 1996). The advent of synchrotron radiation (SR) has added a new dimension to vascular disease diagnosis and has the potential to open new avenues for the implementation of innovative imaging techniques for addressing this issue. Recently, *ex vivo* and *in vivo* imaging using SR has been performed to probe the morphology of the microvasculature of various organ systems (Lu *et al.*, 2010; Ackermann & Konerding, 2015; Velroyen *et al.*, 2014; Kobayashi *et al.*, 2004; Pabst *et al.*, 2014). Since the 1980s, SR imaging has been firstly used in coronary angiography in humans (Rubenstein *et al.*, 1986). The quasi-parallel and monochromatic SR beam has the ability to detect microvessels and delivers a lower radiation dose to patients than conventional computed tomography (CT); thus, SR has the potential for the regular application in clinical practice, and could become a powerful medical diagnostic tool (Zhao *et al.*, 2012; Zhu *et al.*, 2010; Bravin *et al.*, 2013; Longo, 2016; Xi *et al.*, 2015). There have also been extensive experimental analyses of the neurovascular network of the central nervous system in preclinical studies of various pathologies using the BL13W beamline at the Shanghai Synchrotron Radiation Facility in China (Xi *et al.*, 2015; Cao *et al.*, 2015; Zhang *et al.*, 2014*a*), as well as at the Swiss Light Source (SLS) (Heinzer *et al.*, 2006, 2008), SPring-8 (Kidoguchi *et al.*, 2006; Myojin *et al.*, 2007) and ESRF (Risser *et al.*, 2007; Fratini *et al.*, 2015).

In the present study, we focused on recent methodological developments involving SR and their application in the investigation of neurovascular in the central nervous system in preclinical experiments. We emphasize their ability to demarcate in greater resolution the 3D features of the microvasculature of the brain and spinal cord, which can also be analyzed using digital post-processing methods to improve our understanding of the interaction between vascular function and neuronal activity under the physiological and pathological conditions.

2. Characteristics of synchrotron radiation

Synchrotron radiation was first observed in 1947 in an accelerator of the General Electric Synchrotron in the USA (Meuli *et al.*, 2004). When high-energy electrons travel in a storage ring at a speed close to that of light, the direction of the their motion changes under the force of the magnetic field, and electromagnetic radiation known as synchotron radiation is emitted from the circular orbit.

Table 1
Representative third-generation storage ring light sources.

Operation date	SR facility	Electron energy (GeV)	Circumference (m)	Current (mA)	Emittance (nm rad)	Location
1992	ESRF	6	844.4	200	3.8	Europe
1992	ALS	1.5–1.9	196.8	400	6.8	USA
1993	TLS-II	1.5	120	400	10	Taiwan
1994	PLS	2.5	281.82	200	12.0	South Korea
1994	ELETTRA	2–2.4	259.2	300–170	7.0	Italy
1996	APS	7	1104	100	3.0	USA
1997	SPring-8	8	1436	100	3.4	Japan
1998	BESSY II	1.7–1.9	240	270	5.2	Germany
2000	SLS	2.4	288	400	5	Switzerland
2000	ANKA	2.5	110.4	110	70	Germany
2004	CLS	2.9	170.9	300	22.7	Canada
2004	SPEAR-3	3.0	234	500	18	USA
2006	SOLEIL	2.75	354	500	3.75	France
2006	DIAMOND	3.0	561.6	300	2.7	UK
2006	Indus-II	2.5	172.47	300	58	India
2008	SSRF	3.5	432	200–300	3.9	China
2009	PETRA III	6	2304	100	1.0	Germany
2011	ALBA	3	249.6	250	3.7	Spain

There are now more than 50 dedicated synchrotron radiation light sources worldwide, most of which are second and third generation (Bilderback *et al.*, 2005). Table 1 lists representative third-generation synchrotron radiation facilities, the majority of which were constructed with medium-energy electron beams ranging from 2 to 4 GeV. Only the ESRF, PETRA III, SPring-8 and APS are optimized to operate in a high-energy range (6–8 GeV) capable of producing high-intensity X-rays ranging from 10 keV to 50 keV. Other features include a full waveband, high coherence, high directionality, high efficiency, and quasi-parallel and monochromatic beams, especially at high intensities tens of thousands times higher than those achieved by laboratory or medical X-ray sources. Thus, these beams offer high spatial resolution for imaging specimens as well as high time resolution, and greatly reduce the time necessary to obtain experimental data (Hofmann, 1990).

The Shanghai Synchrotron Radiation Facility (SSRF) in China, which houses the most powerful medium-energy light source, uses a 150 MeV LINAC, a booster that can accelerate electrons to 3.5 GeV in half a second and reserve them in the 3.5 GeV electron storage ring with a current of 240 mA and low emittance (3.9 nm rad) (Chen *et al.*, 2014). With the advanced insertion devices installed in the storage ring at SSRF, synchrotron radiation light is characteristic of high photon flux, which is invaluable and available at the X-ray Imaging and Biomedical Application beamline (BL13W1).

The X-ray beam is produced using a 16-pole wiggler, while a double silicon crystal monochromator provides the X-ray beam with energy ranging from 8 to 72.5 keV. The beam cross-section is 45 mm (horizontal) × 5 mm (vertical), and the photon flux density on the sample is approximately 1.5×10^{10} photons mm^{-2} s^{-1}). The Kohzu six-dimensional sample stage and the precision slide rail are flexibly adjustable. In this manner, the optimal sample-to-detector distance and region of

interest can be easily selected. The detector system of the SSRF consists of a 100 μm scintillator and Optique Peter microscope system, and the PCO2000 camera registers 2048 × 2048 pixels. Its performance is optimized across widely used X-ray energies. By using advanced insertion technology, both high-brilliance synchrotron radiation light with 1–5 keV photon energy as well as high-brilliance hard X-rays with 5–60 keV photon energy can be generated, which exhibit similar properties to a high-energy light source (6–8 GeV).

3. Development of SR methodology

3.1. SR absorption contrast imaging

X-ray absorption contrast imaging is achieved by exploiting the different attenuating powers of the materials within a sample (Rabin *et al.*, 2006). This is the most commonly held theory regarding the performance of imaging diagnostic tools that are widely used in medical institutions. Compared with conventional imaging techniques, SR offers several advantages for absorption contrast imaging. The natural collimation of SR makes it possible to select monochromatic radiation for imaging, which enables the tuning of the X-ray energy as a function of the requirements of the examination and a specific sample's characteristics. Consequently, the radiation dose delivered to the specimen can be reduced, which has the potential to translate into clinical application. Moreover, the use of a small spot size and coherent radiation facilitates the high-resolution characterization of different tissue and vessels after contrast agent injection (Suortti & Thomlinson, 2003; Lewis, 1997).

3.2. SR phase contrast imaging

The difference in X-ray attenuation in biological soft tissues is typically weak, and different tissues are rarely differentiated using conventional imaging techniques. In contrast, the phase-contrast imaging becomes visible using SR, was discovered by Fritz Zernike in 1930 and is emerging as an alternative to conventional X-ray radiography (Momose *et al.*, 1996; Zernike, 1955). It allows the detection of weakly differentiated biological soft tissues by picking up phase shifts of the X-ray as it traverses the object (Stevenson *et al.*, 2003; Diemoz *et al.*, 2012). Recently, a variety of X-ray phase-contrast imaging methods have been developed using SR, including (i) propagation-based imaging; (ii) analyzer-based imaging; (iii) interferometric imaging; (iv) grating interferometric imaging; and (v) grating non-interferometric imaging (Lin *et al.*, 2015*a*). At the BL13W1 beamline at SSRF, the propagation-based method has been implemented without the need for additional optics in the SR imaging geometry. The variations in refractive index deviate the X-rays at angles that can be detected by adjusting the detector at a certain distance from the object. In this scenario, edge-enhanced images could be produced, and the interfaces and boundaries in the specimen with different refraction properties were captured. Recently, a grating-based imaging method featuring absorption grating and phase grating have been established at BL13W1 (Xi *et al.*, 2012).

3.3. SR microtomography

Microtomography is a non-destructive technique that is widely used for 3D imaging of sample morphology, and quantitative information describing sample structure can also be obtained (Larrue *et al.*, 2011; Lu *et al.*, 2015). SR microtomography (SR-μCT) offers several advantages over conventional methods. SR allows high-resolution acquisition of the 3D morphology of a sample at the micrometre level as well as a quantitative evaluation of the linear attenuation coefficient distribution within the sample. Furthermore, SR yields reconstructed CT images that are free of beam-hardening artifacts (Tapfer *et al.*, 2014). SR phase-contrast microtomography, a complement to absorption microtomography, is a novel imaging modality with extensive applications in biomedicine recently, especially for the study of vessel structure without the use of a contrast agent (Hagen *et al.*, 2015; Hwu *et al.*, 2004). *PITRE* software, developed by Chen, is freeware that supports SR-based phase-sensitive X-ray imaging and is used for phase retrieval and imaging reconstruction at the BL13W1 facility (Chen *et al.*, 2012).

3.4. SR microangiography

Microangiography using SR as the light resource yields superior image quality and permits detailed high-resolution imaging of microvessels down to a 10 μm diameter *in vivo* (Kidoguchi *et al.*, 2006; Yamashita *et al.*, 2002; Lundström *et al.*, 2012; Tang *et al.*, 2011; Shirai *et al.*, 2013). SR microangiography has a high temporal resolution and a short exposure time on the order of milliseconds, allowing for a high flux and narrow pulse time appropriate for real-time dynamic imaging of microvessels within intact organ systems (Shirai *et al.*, 2009). Furthermore, the high-energy X-ray beam emitted from the synchrotron storage ring produces extremely bright light that can penetrate thick tissue and create high-contrast, blur-free images of a sample.

There are two approaches to using SR microangiography for vascular imaging: *K*-edge subtraction angiography and single-energy temporal subtraction angiography. With *K*-edge subtraction, imaging large animals is possible, but resolution is compromised. The second approach, which enhances a contrast agent contained in blood vessels using single-energy monochromatic SR, facilitates high-resolution imaging at the expense of the imaging field of view (Peterzol *et al.*, 2005).

4. Use of SR in neurovascular imaging

The structure of the neurovascular network in the central nervous system is more complicated than that of any other known biological organ. At present, the relationship between neural activity and vascular function has not been fully elucidated. Fine-grained descriptions of the morphology of the neurovascular network at the micrometre or sub-micrometre level may underlie pathological changes or developmental disorders, and as such should be characterized. One advantage of SR is its ability to characterize the 3D morphology of a specimen without sectioning when combined with a tomo-

graphy algorithm. Additionally, SR enables the differentiation of vessels without the use of a contrast agent, and identifies similar structures at high resolution. Moreover, this technique permits the visualization of microvasculature *in situ* under natural physiological conditions (Shirai *et al.*, 2009). In this section, we focus primarily on evaluating the application of SR for ultra-high-resolution imaging and neurovascular morphology microtomography under physiological and various pathological conditions.

4.1. Cerebral vascular system

4.1.1. *In vivo* functional imaging. Conventional techniques such as MRA and CTA are commonly used in the detection of large superficial pial vessels, whereas smaller and deeper arterioles are below the detection limit of conventional imaging techniques. Undoubtedly, this limitation is detrimental to disease diagnostics and prognosis at very early stages. With the aid of SR microangiography (SRA), microvascular changes correlating with many cerebral disorders are being intensely identified and studied. Early experiments aimed to validate SR as an effective method for measuring the diameters of small cerebral microvessels (Zhang *et al.*, 2014*b*). Currently, numerous investigations study the microstructure and function of these smaller cerebral vessels, primarily in rodents (Guan *et al.*, 2012; Yuan *et al.*, 2012; Liu *et al.*, 2010) (Fig. 1), and occasionally in larger animals.

SRA makes possible the study of the dynamic autoregulatory responses of both pial and penetrating perforating microvascular beds simultaneously, without magnification artifacts or focal blurring during pathological conditions such as hypoxia, hypertension, hyperglycemia, stroke, subarachnoid hemorrhage or cerebral aneurysms and aging related disease (Guan *et al.*, 2012; Yuan *et al.*, 2012; Liu *et al.*, 2010; Zhao *et al.*, 2015; Wang *et al.*, 2016; Mu *et al.*, 2016; Lu *et al.*, 2012; Lin *et al.*, 2015*b*). It is common knowledge that angiogenesis exhibits an important compensatory pattern in ischemic diseases to improve the blood supply to ischemic regions. Lu *et al.* (2012) employed SRA as an effective auxiliary method to observe angiogenesis *in situ* in conjunction with different therapies, including gene overexpression, to treat ischemic stroke in animal models. These studies provide potent support for the evaluation of the curative effects of novel therapies using these tools. Furthermore, Lin *et al.* (2015*b*) exploited a novel approach to study the elasticity of the sub-cortical vasculature after cerebral ischemia in rats using an SRA-based spatio-temporal analysis of contrast density in arterial cross sections. Their findings open new avenues in the real-time dynamic multi-functional imaging of cerebral structures at high resolution in living organisms. However, at present, microangiography images in the neuroscience field remain restricted to 2D representations, which limited the precise vessel quantitative analysis. Naturally, for biomedical applications, full four-dimensional (4D) spatiotemporal imaging of a living specimen is highly desirable. With the development of *in vivo* SR X-ray cine-tomography as a 4D imaging technique, it will be possible to study real-time dynamics accurately in small animals at a micrometre spatial resolution and sub-second time resolution.

4.1.2. High-resolution 3D visualization. In mammals, the complex functions of the brain depend on the fine anatomical architecture of enormous numbers of vessels and their connections. Cerebral perfusion is thus essential for the function of the central nervous system. Notably, 3D high-resolution imaging and deciphering the structural parameters of the cerebrovascular network at both the global and local levels are undoubtedly important prerequisites for the direct assessment of neurovascular disease models.

In a recent study, our group set out to define ultra-high-resolution 3D digitalized angioarchitectural maps of the rodent brain using SR phase-contrast imaging (SR-PCI) (Zhang *et al.*, 2015). We reconstructed multi-angle 3D digital

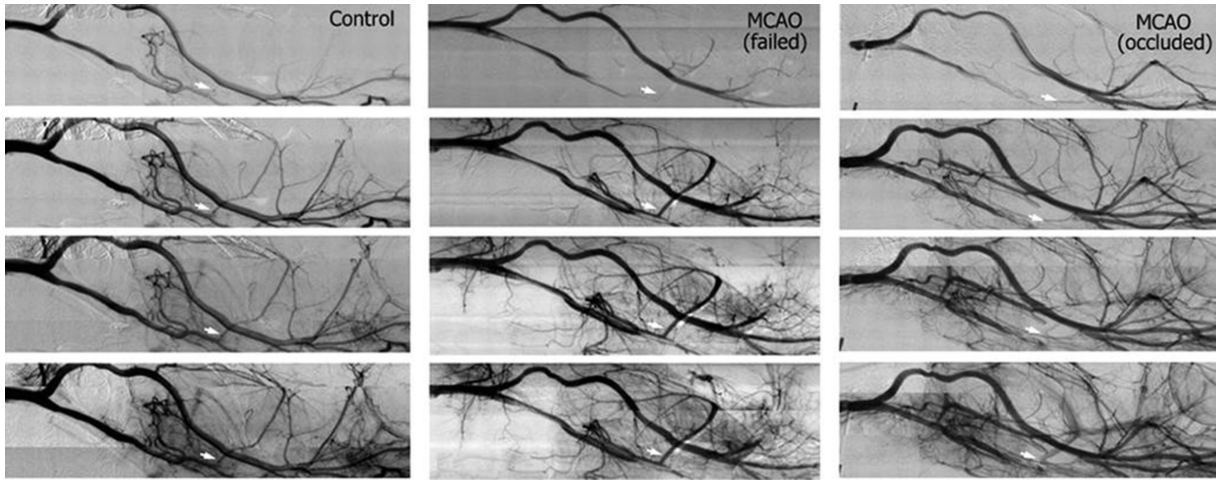

Figure 1
Synchrotron radiation angiography images were taken immediately after the injection of contrast agent. The images shown (top to bottom) were taken at 50 ms, 125 ms, 200 ms and 275 ms. Normal cerebral vasculature (left); unsuccessful middle cerebral artery occlusion (MCAO) using 4-0 suture without coating (center) and successful MCAO using silicone-coated 4-0 suture (right) are detected. Reproduced with permission from Guan *et al.* (2012). Copyright (2012), Wolters Kluwer Health Inc.

anatomical images, revealing the spatial network of vessels at the whole brain level and in specific brain regions, including the hippocampus, pre-frontal cortex and corpus striatum. At the cellular level, grating interferometry phase and conventional absorption SR-μCT setups were used to investigate the 3D microstructure of the human cerebellum, including blood vessels and different strata (Georg *et al.*, 2010). Individual Purkinje cells were visualized without the use of staining or contrast agents under this imaging setup, demonstrating the superiority of the SR technique for the 3D micro-characterization of microvasculature or individual cells in even the most complex normal brain tissues at the micrometre scale.

Detecting alterations of the microvasculature either qualitatively or quantitatively under diverse pathogenic conditions may provide crucial clues to pathogenic mechanisms. Heinzer *et al.* (2006) initially proposed a hierarchical microimaging method for multiscale analysis of large microvascular networks in brain vascular corrosion casts. In particular, precise anatomical context for regions of interest (ROIs) scanned for 3D morphology could be nondestructively obtained by SR-μCT at a pixel resolution of 1.4 μm. 3D vessel parameters such as vessel volume, thickness, spacing and connectivity density were calculated sequentially, opening new possibilities to study vessel architecture and vascular alterations in diverse pathological models (Fig. 2).

Additionally, Heinzer *et al.* (2008) further employed this SR-μCT 3D imaging technique in combination with vascular network analysis tools to characterize brain angioarchitecture in transgenic mice overexpressing human VEGF165. Based on 3D vessel morphometry analysis of ROIs, they hypothesized that the smallest 'angiogenic quantum' – the final, stable result of angiogenesis and subsequent remodeling – is not a single microvessel but a complete micro-network. Undoubtedly, this novel technique could also be applied to other experimental systems and may thus contribute to improving our understanding of vascular remodeling in terms of mammalian evolution and pathology. Stolz and co-workers (Stolz *et al.*, 2011) evaluated subacute superior sagittal sinus (SSS) thrombosis in rats using micro-, nano- and synchrotron-based micro-CT. The 3D SR renderings distinctly demonstrated a newly formed network of microvessels ('venogenesis') draining the bridging veins in the SSS at six weeks after thrombosis (Fig. 3).

Similarly, Risser *et al.* (2009) described the application of the SR 3D technique for functional vessels in a systematic in-depth quantitative study of angiogenesis in the primate cortex that involved the identification of microvascular components as well as their automatic numerical digitalization and extraction via massive 3D image analysis and post-treatments. Over the entire cortical depth, increases in vascular volume, exchange surface and vessel length were revealed in adult marmosets compared with newborns, indicating that intensive remodeling of micro-vascular patterns was accompanied with neural connectivity plasticity during postnatal cortical maturation.

Current bio-medical imaging studies also aim to detect brain tumors and micrometastases in early stages. SR-PCI techniques such as grating interferometry were employed by Pfeiffer *et al.* (2007) to generate postmortem 3D reconstructions of a rat brain bearing a 9L gliosarcoma, wherein tumor location and important brain structures such as the cerebellum were clearly identified.

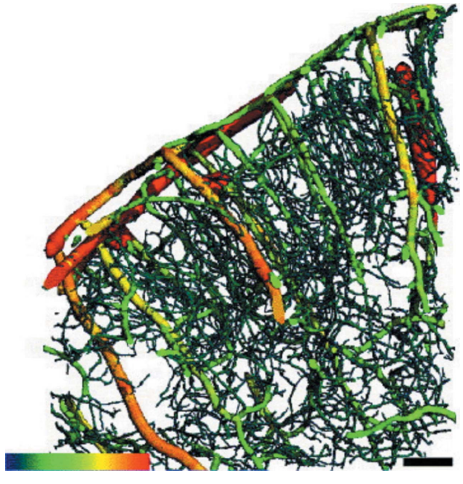

Figure 2
Portion of microvasculature from the left frontal cortex. The color coding reflects the vessel thickness, ranging in the current example from about 5 A m (dark green) to 30 A m (red). Scale bar: 100 A m. Reproduced with permission from Heinzer *et al.* (2006). Copyright (2006), Elsevier.

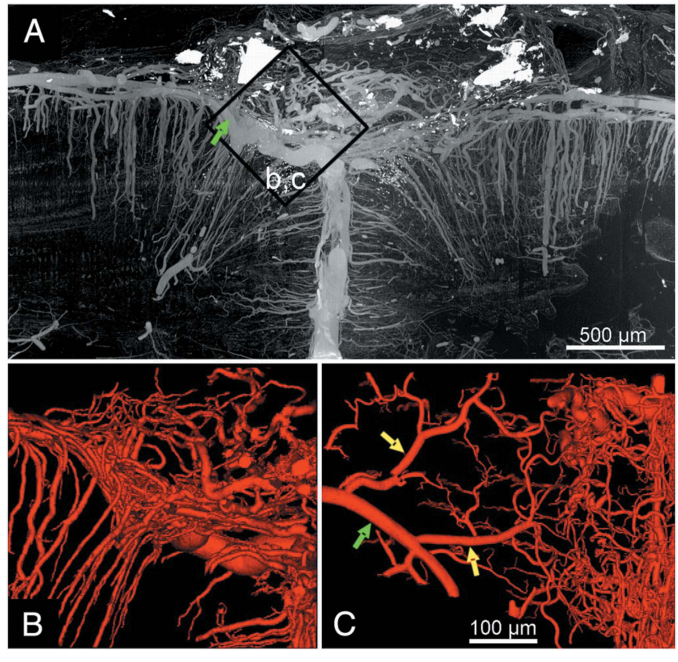

Figure 3
Synchrotron-based micro-computed tomography. (A) Three-dimensional maximum intensity projection clearly showing the vascular network in the superior sagittal sinus six weeks after thrombosis (the green arrow demonstrates the cortical vein). (B and C) Detailed view in different spatial projections showing the connectivity of the microvascular network with cortical veins (the green arrow demonstrating the cortical vein, yellow arrows showing the branching veins connecting the newly formed microvessels). Reproduced with permission from Stolz *et al.* (2011). Copyright (2011), Elsevier.

Other PCI techniques such as in-line phase-contrast (ILPC) and grating-based phase-contrast imaging are effective enough to provide intuitive visualization of breast cancer micrometastases in an *ex vivo* mouse brain (Huang *et al.*, 2015). These two SR-PCI techniques can differentiate the abnormal tumorous microstructures induced by micrometastasis from the surrounding normal tissues. In our recent study, we developed an ILPC imaging technique for use in ischemic stroke and provided 3D evidence for angiogenesis (Zhang *et al.*, 2014*a*; Connor *et al.*, 2009). In addition, amyloid plaques indicative of Alzheimer's disease (AD) have been visualized as small focal masses in the cortex and hippocampus, which are invisible by conventional X-ray absorption imaging techniques due to their small size and weak absorptive properties, in a mouse AD model using SR analyzer-based imaging and grating interferometric methods (Connor *et al.*, 2009; Pinzer *et al.*, 2012). Hence, SR-PCI seems poised to emerge as a powerful tool for depicting the 3D arrangement of the cerebral vasculature in conjunction with a global-local perspective, which may further benefit the development of therapeutic angiogenesis as a clinical tool for application in various neurovascular diseases.

In 2010, Li *et al.* (2010) developed a micro-optical sectioning tomography (MOST) system based on Golgi staining that generates a 3D brain-wide map of neural circuits at a mesoscale level. The morphology and spatial location of neurons and traces of neurites could be clearly distinguished. Furthermore, a recent study by Kasthuri *et al.* (2015) developed automated technologies to explore the structure of neural circuits at nanometre resolution using scanning electron microscopy as well as subsequently generated a saturated 3D reconstruction of a sub-volume of mouse neocortex in which all cellular objects and many sub-cellular components were rendered and itemized (Fig. 4).

These two studies open superb prospectives for 3D tomography in neural micro-structure at ultra-high resolution, which lay the foundation to elucidate the in-depth physical properties of brain tissue. However, compared with SR-PCI, these techniques demand sectioned brain tissues, which are more frangible to external force disruption and may affect the

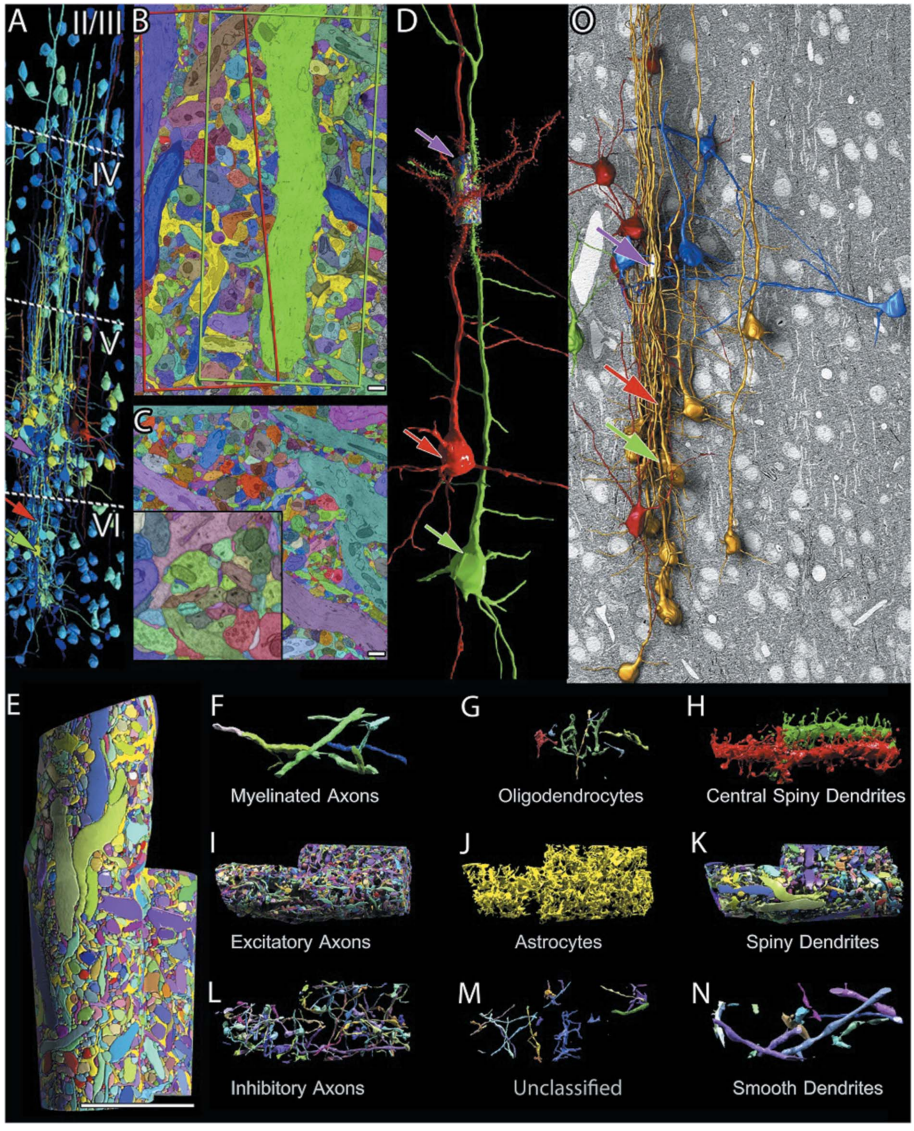

Figure 4
Multi-scale reconstruction in neocortex. (A) Cortical neuronal somata reconstruction to aid in cortical layer boundaries (dotted lines) based on cell number and size. Large neurons are labeled red; intermediate ones are labeled yellow; and small ones are labeled blue. The site of the saturated segmentation is in layer V (pink arrow). These two-layer VI pyramidal cell somata (red and green arrows) give rise to the apical dendrites that form the core of the saturated cylinders. (B) A single section of the manually saturated reconstruction of the high-resolution data. The borders of the cylinders encompassing the 'red' and 'green' apical dendrites are outlined in this section as red and green quadrilaterals. This section runs through the center of the 'green' apical dendrite. (C) A single section of a fully automated saturated reconstruction of the high-resolution data. The higher magnification view (lower left inset) shows 2D merge and split errors. (D) The two pyramidal cells (red and green arrows) whose apical dendrites lie in the centers of the saturated reconstructions. Dendritic spines reconstructed in the high-resolution image stack only. (E) The saturated reconstruction volume. (F–N) The 'parts list' of the saturated volume. (O) Reconstruction of 30 dendrites contained within cylinder 1 (pink arrow) that were traced back to their cell bodies. These dendrites were predominantly apical dendrites of pyramidal cells (gold), several basal dendrites of pyramidal cells (blue), and in one case both a branch of the apical and a basal dendrite branch of the same pyramidal cell entered the volume (green) and a small number of non-pyramidal cell dendrites (red). The somata of the red and green apical dendrites that lie at the centers of saturated reconstruction are shown by the red and green arrows. Scale bars: 1 μm for (B) and (C); and 7 μm for (E). Reproduced with permission from Kasthuri *et al.* (2015). Copyright (2015), Elsevier.

sequent 3D reconstruction images in a detrimental way. In the future, the combination of nerve staining and SR techniques will aid in the 3D mapping of neural circuits and vascular network simultaneously within the same intact brain samples at the micrometre, or even nanometre, level.

4.2. Spinal cord vascular system

The spinal cord is the main pathway for information connecting the brain and peripheral nervous system. The function and viability of the spinal cord are critically dependent on the efficient delivery of oxygen and glucose through the microvasculature which is characterised by unique 3D morphology (Mori *et al.*, 1994, 1996; Lu *et al.*, 2010).

4.2.1. *In vivo* function imaging. With regard to the *in vivo* visualization of the microvasculature in the central nervous system using SR, there has been broad application in the brain (Zhang *et al.*, 2014*b*). However, the anatomical features of the spinal cord have made the implementation of *in vivo* imaging in the study of the living mouse spinal cord a challenging task. The anatomical location of the spinal cord, which is close to the lungs and heart, inevitably generates significant movement artifacts that causes the failure of the *in vivo* imaging of the spinal cord microvasculature. To address this issue, a proper spine fixing device designed by our research group to restrict the spine motion is being tested.

4.2.2. High-resolution 3D visualization. Until recently, with the application of micro-CT, the 3D morphology of the spinal cord vessel could be detected, and it has been used in different animal models in preclinical experiments such as in chronic spinal cord injury (Cheng *et al.*, 2015; Long *et al.*, 2014) and the acute traumatic injury model (Long *et al.*, 2014) to elucidate the underlying mechanism involved in the vessels that aid in developing novel methods for this treatment (Figley *et al.*, 2014). However, vessels with diameters less than 20 µm could not be captured due to the technique's limited imaging resolution, thus restricting its further application (Hu *et al.*, 2012*a*). SR offers a unique platform for the characterization of the microvasculature within the intact organ down to the micrometre level. Our group first employed this method to visualize the 3D morphology of the spinal cord microvasculature in a rat model after contrast agent injection (Fig. 5) (Hu *et al.*, 2014).

A clear and precise configuration of the spinal cord microvasculature was provided by this tool. The intrinsic arteries of the spinal cord, including a central and a peripheral vascular system, were vividly detected. Furthermore, the typical butterfly shape of the spinal cord microvasculature in the gray matter was outlined and was more intense than that of the white matter, indicating that the neurons located in the gray matter have higher oxygen and nutritional metabolic demands.

Additionally, we find that SR-µCT could achieve higher resolution in 3D vascular imaging compared with micro-CT, and the smallest vessel that could be distinguished was approximately 7.4 µm in diameter (Hu *et al.*, 2014). When the rat suffered from traumatic injury, the vessel numbers in the damaged spinal cord area decreased significantly, and the injury was not constrained at the epicenter; and it will expand rostrally and caudally along the spinal cord. This result reveals that the structural destruction and volumetric collapse of the microvasculature were directly induced by the acute trauma. This is a devastating event; the importance of blood supply protection should be emphasized in the spinal cord injury process due to the unique hallmark of the circulation system. In addition to SR-µCT-based absorption imaging, X-ray in-line phase-contrast computed tomography (IL-XPCT) was employed. The 3D angioarchitecture of the spinal cord both at normal (Hu *et al.*, 2012*b*) and injury status (Hu *et al.*, 2015) were successfully obtained via IL-XPCT without the use of a contrast agent.

These results demonstrate that both phase-contrast imaging and absorption imaging-based SR have the capability to image pathological changes in small arteries and may provide crucial clues to illuminate the pathogenic mechanisms underlying this neurovascular diseases. Takashima *et al.* (2015) have also applied these tools to visualize the microstructure of polyglycolic acid scaffolds and to evaluate their degradation after implantation into injured spinal cords. These studies revealed that SR is a versatile technique with many functions and applications in different fields.

The interaction between nerves and blood vessels in the central nervous system is more complicated than is revealed by our imaging. As a result, much of the fine structure of the neurovascular network remains largely unexplored. Another

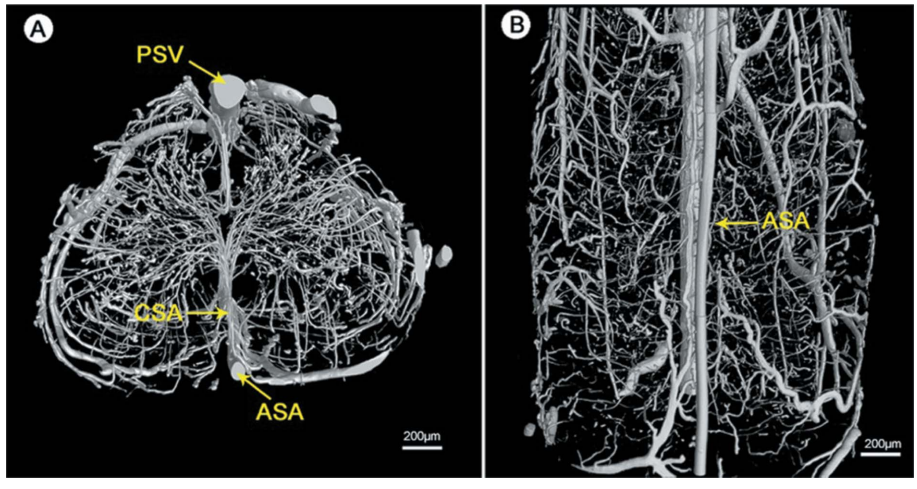

Figure 5
Illustration of the 3D microvasculature of the rat spinal cord by SR-µCT. (A) Transverse view of the angioarchitecture. (B) Top view of the angioarchitecture. Both (A) and (B) show the primary blood supply system of the spinal cord, including the anterior spinal artery (ASA), the central sulcus artery (CSA) and the posterior spinal vein (PSV). Scale bar = 200 µm. Reproduced with from Hu *et al.* (2014).

important application of this method is the investigation and visualization of the interaction between neural and vessel activity within the intact organism. It is now possible, with the aid of SR, to visualize the 3D morphology of the vasculature and neuronal systems in the mouse spinal cord at high resolution. These studies have produced a plethora of novel and unexpected findings regarding neural and vascular activity under physiological or pathological conditions. They have also revealed demarcated tissue borders at the gray or white matter boundaries of the spinal cord. Based on Golgi staining, our group performed preliminary investigation of the application of these imaging techniques to the visualization of the 3D morphology of the neural networks in the spinal cord. Due to the low resolution of our CCD, only the soma of the neurons could be detected.

5. SR imaging data post-processing

5.1. 3D vascular quantitative analysis

To quantitatively analyze vascular structure morphology in 3D, the vessel tree analysis model for vascular structure characterization was used. After the vasculature was segmented from the parenchyma, the following protocol for vascular morphological parameter calculation was performed. (i) Vectorization, a skeletonization based on voxel erosion (Cornea *et al.*), was used to automatically extract the midline of the vessel. (ii) Once the midline had been successfully extracted, numerous parameters needed for vascular network quantification, such as vessel length, vessel diameter, vessel volume, vessel volume fraction and vessel bifurcation for each segment in the ROI, could be systematically analyzed (Cornea *et al.*, 2005). A vessel segment was defined as a section of the vascular network lying between two vessel bifurcation points. The vessel length was measurement by the sum of the distances between the two bifurcation points. A 3D Euclidean distance map of the vasculature was evaluated as described previously using the Chamfer Map module in VG Studio *Max*, *Image Pro Analyzer 3D* and *Amira* imaging software to determine the 3D vessel radius. The vessel diameter was calculated from the vessel radius (R_m) as the mean radius R_m leading to the mean diameter ($D = 2R_m$). The vessel volume fraction represents the ratio between the number of voxels belonging to a given vessel and the total number of voxels in the biological tissue (Lang *et al.*, 2012).

5.2. 3D virtual micro-endoscopy

In addition to the quantitative analysis of 3D vasculature, more in-depth 3D data exploration can be conducted. For instance, virtual cerebrovascular micro-endoscopy can be performed based on SR data (Fig. 6) (Zhang *et al.*, 2015).

This process includes path planning and real-time rendering, and enables the simulation of virtual camera recordings moving dynamically through a targeted vessel lumen. By setting the position and orientation of the camera along the pathway within the vessel, 'virtual flight' enables the visualization of vessels from this novel perspective. This

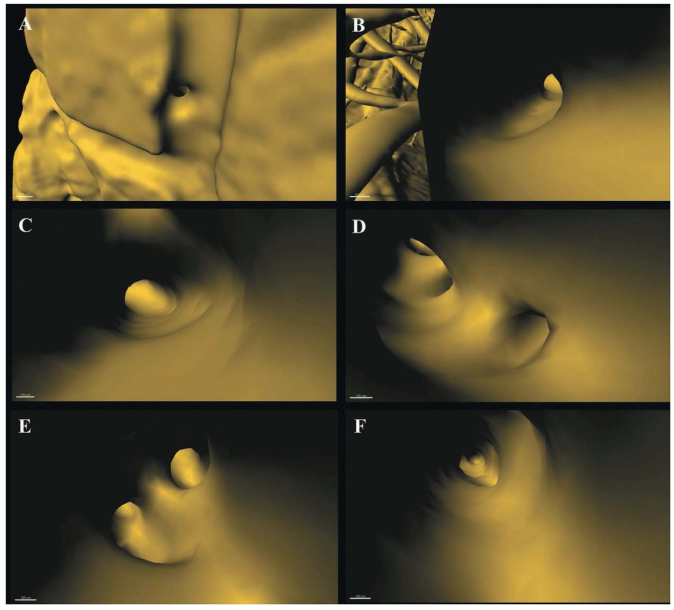

Figure 6
Virtual 3D micro-endoscopy of a targeted vessel. (A) Orientation of the vessel, with successive pathway tracing in (B) to (F). The endovascular micro-structure is clearly discernible. Scale bars: 100 µm. Reproduced from Zhang *et al.* (2015).

innovation will make it possible to localize relevant blood vessels and to non-invasively measure pathological changes in various models of vascular diseases. It also provides a potential method for monitoring and targeting drug delivery during functional vascular mapping studies.

5.3. Blood flow simulation

Understanding the 3D structure of microvasculature alone is often not sufficient because the regulation of organ perfusion is closely related to the alteration of vascular morphology via a process termed autoregulation. Recently, thanks to the acquisition of low-resolution images of spinal cord vessels obtained via conventional methods, several studies have examined the parameters of vasculature hemodynamics. The high-resolution morphology law data derived via SR have made it possible to relate the geometric information obtained from vascular images to the functional properties of vascular circulation. The morphology–function relationship of the vascular tree allows us to simulate the dynamic blood flow in the extracted imaged vascular system. The pressure distribution within the arteries as well as changes in flow velocity can be detected (Fig. 7). Additionally, anatomical, hemodynamic and functional information could be obtained from SR images and represents an important new step in the diagnosis of specific vascular diseases (Holme *et al.*, 2014; Zhang *et al.*, 2011).

5.4. Pseudo color display

The SR imaging technique provides massive amounts of high-resolution raw imaging of blood vessels within intact organs. However, the 3D nature and high complexity of the

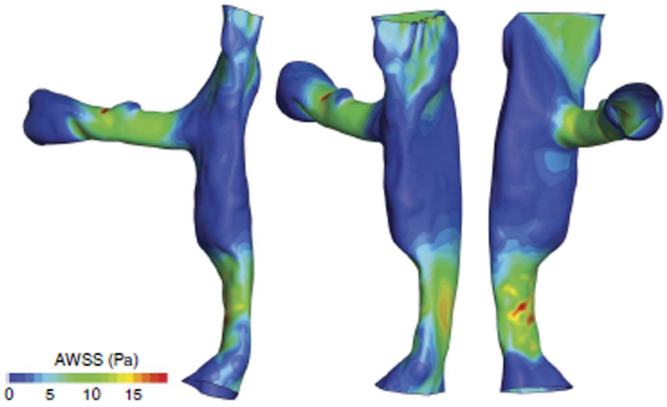

Figure 7
Blue-colored regions show similar AWSS (time-averaged wall shear stress) as healthy arteries (<5 Pa). Green-colored regions are larger than those observed in the healthy body (7–12 Pa). Yellow- and red-colored regions indicate markedly stenosed areas (>13 Pa), with AWSS values being one order of magnitude higher than those typically observed in the healthy vascular system. The length along the vessel section is 7.5 mm. Reproduced with permission from Holme *et al.* (2014). Copyright (2014), Springer Nature.

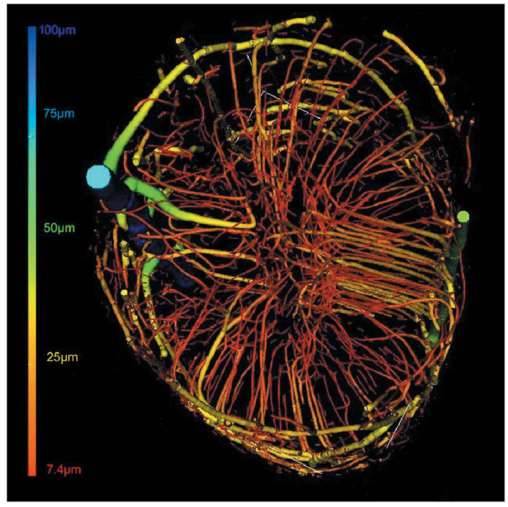

Figure 8
3D pseudo-colored microvasculature of the spinal cord. The color bar indicates the association with different vessel diameters. Reproduced from Cao *et al.* (2015).

vasculature complicates the recognition and analysis of the vessel network. To analyze the vascular connectivity of the central nervous system in a tractable manner, the local vascular features are automatically labeled using different colors. This methodology has already been validated for brain imaging (Ghanavati *et al.*, 2014); the length, diameter and relational features as well as connections representing each of the vessel segments in the spinal cord could be labeled with an anatomical name using different colors, thereby enabling a detailed and high-quality 3D analysis. Additionally, the spinal cord microvasculature illuminated by segmentation could be color-coded by vessel thickness (Fig. 8) (Cao *et al.*, 2015), systematically illustrating the structural characteristics of vasculature and tracing variations in target vascular.

5.5. Virtual histology

In addition to imaging entire organs, morphology may also be determined for macroscopic physiological slices. Using the techniques presented here, the 3D data generated by SR-CT are directly converted into voxel data volumes and can be modified into thousands of serial virtual slices at multiple thicknesses or orientations, thereby allowing the region of interest of the object to be virtually manipulated (Qu *et al.*, 2015). This technique allows us to explore the otherwise inaccessible morphology of an object, increasing our ability to recognize patterns in a nondestructive manner that can be used to obtain the complete 3D structure of a specimen.

6. Limitations of current research and future directions

CLARITY is a novel tissue clearing technique which processes intact biological tissues into a nanoporous hydrogel-tissue hybrid, thus preserving anatomical structures, proteins and nucleic acids (Kwanghun *et al.*, 2013). The hydrogel-based structures present transparent states after the disposal of lipids. Popular with researchers in neuroscience and developmental biology, this technique provides an ideal way to visualize the intact mouse brain and spinal cord in the central nervous system (Du *et al.*, 2018). Unfortunately, a considerable time investment is required from tissue clearing to the acquisition of imaging data. Furthermore, large and thick samples pose a sizable challenge in achieving an optimized level of transparency for successive imaging (Kazuki *et al.*, 2014). The CLARITY imaging process, involving a two-photon microscope to generate the three-dimensional fluorescent images, is not feasible for high-resolution 3D volume imaging approaches due to the current limitations. The culmination of factors, namely poor penetration depth limiting the scale of samples, a complicated processing procedure and the time-consuming nature of image generation requiring point by point scanning, warrant the need for a simplified and efficient alternative (Kwanghun *et al.*, 2013; Ragan *et al.*, 2012; Raju *et al.*, 2014). In addition, attention needs to be paid to monitor the potential phototoxicity when conducting laser tomography. Conversely, the preparation for SR-μCT is not complicated with the ability to rapidly scan the intact sample thus acquiring ultra-high-resolution 3D images due to the monochromaticitic, high brightness, high collimation, high polarization SR X-rays (Luo *et al.*, 2019).

There are many advantages of the current imaging approach for neurovascular detection. However, the technical restrictions of today's SR methodology prevent its further application. Most apparent physically is that the SR apparatus is large, which may restrict availability to all academic research laboratories and limit its application in clinical institutions. Future work should ameliorate and miniaturize the SR apparatus and optimize the scanning parameters such that they are suitable for clinical application. Furthermore, due to the limited image field of the detector, SR beam light is not ideal for use in large animals. Despite the difficulties of this

technique, satisfactory results have been achieved with intravenous KEDSA dual-energy CT, and *in vivo* imaging of the cerebral vascular network in large animals has been performed successfully (Schültke *et al.*, 2010, 2011). This study indicated that SR can be employed for neurovascular research and that it has the potential to translate from use in larger animals to clinical practice. In addition, high-resolution imaging necessitates long scanning and exposure times, which inevitably results in the delivery of higher radiation doses to the specimen. Current efforts must work to optimize imaging parameters and decrease the radiation doses required prior to application in the medical field. SR angiography is an important approach to studying the brain vasculature in real time and dynamically *in vivo*; however, currently it cannot make 3D images. In theory, it will be possible to perform fast and complete 4D spatiotemporal SR phase-contrast imaging of living rodents in the near future. If the scanning time is decreased significantly, the radiation dose will also decrease accordingly. Another challenge is the simultaneous 3D visualization and quantitative analysis of both the microvascular network and the neuronal system. Recent studies have verified that SR-μCT allowed the 3D simultaneous visualization of the single neuron and vessel network in mouse spinal cord on the sub-micrometre scale; however, the complex interaction mapping needs to be further elucidated in depth (Fratini *et al.*, 2015). The presented method will be a promising platform in a broad range of future life science to break through the traditional applications, such as 3D printing, tissue engineering, drug discovery, and the possible combination with other SR microspectrum analysis methods to analyze biochemical and morphological characteristics in depth.

7. Conclusion

Undoubtedly, SR X-ray imaging has proven to be a powerful tool for exploring neurovascular network morphology. Coupled with the computerized tomography, SR-μCT allows us to non-destructively image the microvasculature network at the sub-micrometre scale. Additionally, by way of SR phase-contrast μCT, the detection and identification of changes in microvessels can be achieved without the use of a contrast agent, offering a new platform and a powerful imaging technique for better understanding the complex biological interactions between vascular function and neuronal activity in the central nervous system under both physiological and pathological conditions.

Acknowledgements

We thank our collaborators and colleagues working in the field of biomedical applications of synchrotron radiation for making their latest results available. We are very grateful to the staff of Shanghai Synchrotron Radiation Facility for their kind help in preparing this manuscript. We thank the authors, editors and publishers for their kind permission to reprint illustrations of previously published results.

Funding information

The following funding is acknowledged: National Natural Science Foundation of China (grant Nos. 81501025, 81371956, 81171698, 81672174, 81730068, 81472072, 81171699, 61772556); Natural Science Foundation of Hunan Province (grant Nos. 2016JJ3174, 2017JJ2330); Science Foundation of Xiangya Hospital for Young Scholar (grant No. 2017Q1); Changsha Science and Technology Plan Key Project (grant No. kq1801066); The Science and Technology Commission of Hunan Province of China (grant No. 2017SK2061).

References

Ackermann, M. & Konerding, M. A. (2015). *Methods Mol. Biol.* **1214**, 49–66.
Bilderback, D. H., Elleaume, P. & Weckert, E. (2005). *J. Phys. B At. Mol. Opt. Phys.* **38**, S773–S797.
Bravin, A., Coan, P. & Suortti, P. (2013). *Phys. Med. Biol.* **58**, R1–R35.
Cao, Y., Wu, T., Yuan, Z., Li, D., Ni, S., Hu, J. & Lu, H. (2015). *Sci. Rep.* **5**, 12643.
Chen, R.-C., Dreossi, D., Mancini, L., Menk, R., Rigon, L., Xiao, T.-Q. & Longo, R. (2012). *J. Synchrotron Rad.* **19**, 836–845.
Chen, R. C., Liu, P., Xiao, T. Q. & Xu, L. X. (2014). *Adv. Mater.* **26**, 7688–7691.
Cheng, X., Long, H. Q., Chen, W. L,, Xu, J. H., Huang, Y. L. & Li, F. B. (2015). *Neurosci. Lett.* **606**, 106–112.
Connor, D. M., Benveniste, H., Dilmanian, F. A., Kritzer, M. F., Miller, L. M. & Zhong, Z. (2009). *Neuroimage*, **46**, 908–914.
Cornea, N. D., Silver, D., Yuan, X. S. & Balasubramanian, R. (2005). *Vis. Comput.* **21**, 945–955.
Diemoz, P. C., Bravin, A. & Coan, P. (2012). *Opt. Express*, **20**, 2789–2805.
Du, H., Hou, P. H., Zhang, W. B. & Li, Q. Y. (2018). *Exp. Ther. Med.* **16**, 1567–1576.
Figley, S. A., Khosravi, R., Legasto, J. M., Tseng, Y. F. & Fehlings, M. G. (2014). *J. Neurotrauma*, **31**, 541–552.
Fratini, M., Bukreeva, I., Campi, G., Brun, F., Tromba, G., Modregger, P., Bucci, D., Battaglia, G., Spanò, R., Mastrogiacomo, M., Requardt, H., Giove, F., Bravin, A. & Cedola, A. (2015). *Sci. Rep.* **5**, 8514.
Georg, S., Timm, W., Irene, Z., Franz, P., Felix, B., Christian, D., Simon, R., Elena, R. & Bert, M. (2010). *J. R. Soc. Interface*, **7**, 1665–1676.
Ghanavati, S., Lerch, J. P. & Sled, J. G. (2014). *Neuroimage*, **95**, 117–128.
Guan, Y., Wang, Y., Yuan, F., Lu, H., Ren, Y., Xiao, T., Chen, K., Greenberg, D. A., Jin, K. & Yang, G. Y. (2012). *Stroke*, **43**, 888–891.
Hagen, C. K., Maghsoudlou, P., Totonelli, G., Diemoz, P. C., Endrizzi, M., Rigon, L., Menk, R. H., Arfelli, F., Dreossi, D., Brun, E., Coan, P., Bravin, A., De Coppi, P. & Olivo, A. (2015). *Sci. Rep.* **5**, 18156.
Heinzer, S., Krucker, T., Stampanoni, M., Abela, R., Meyer, E. P., Schuler, A., Schneider, P. & Müller, R. (2006). *Neuroimage*, **32**, 626–636.
Heinzer, S., Kuhn, G., Krucker, T., Meyer, E., Ulmann-Schuler, A., Stampanoni, M., Gassmann, M., Marti, H. H., Müller, R. & Vogel, J. (2008). *Neuroimage*, **39**, 1549–1558.
Hofmann, A. (1990). *Characteristics of Synchrotron Radiation*, CERN. Report, pp. 115–141. CERN, Geneva, Switzerland.
Holme, M. N., Schulz, G., Deyhle, H., Weitkamp, T., Beckmann, F., Lobrinus, J. A., Rikhtegar, F., Kurtcuoglu, V., Zanette, I., Saxer, T. & Müller, B. (2014). *Nat. Protoc.* **9**, 1401–1415.
Hu, J., Cao, Y., Wu, T., Li, D. & Lu, H. (2015). *Spinal Cord*, **53**, 585–590.
Hu, J. Z., Cao, Y., Wu, T. D., Li, D. Z. & Lu, H. B. (2014). *Med. Phys.* **41**, 101904.

Hu, J. Z., Wu, T. D., Zeng, L., Liu, H. Q., He, Y., Du, G. H. & Lu, H. B. (2012*b*). *Phys. Med. Biol.* **57**, N55–N63.
Hu, J. Z., Wu, T. D., Zhang, T., Zhao, Y. F., Pang, J. & Lu, H. B. (2012*a*). *J. Neurosci. Methods*, **204**, 150–158.
Huang, S., Kou, B. Q., Chi, Y. Y., Xi, Y., Cao, Y. X., Cui, W. L., Hu, X., Shao, Z. M., Guo, H., Fu, Y., Xiao, T., Sun, J., Zhao, J., Wang, Y. & Wu, J. (2015). *Sci. Rep.* **5**, 9418.
Hwu, Y., Tsai, W. L., Je, J. H., Seol, S. K., Kim, B., Groso, A., Margaritondo, G., Lee, K. H. & Seong, J. K. (2004). *Phys. Med. Biol.* **49**, 501–508.
Kasthuri, N., Hayworth, K. J., Berger, D. R., Schalek, R. L., Conchello, J. A., Knowles-Barley, S., Lee, D., Vázquez-Reina, A., Kaynig, V., Jones, T. R., Roberts, M., Morgan, J. L., Tapia, J. C., Seung, H. S., Roncal, W. G., Vogelstein, J. T., Burns, R., Sussman, D. L., Priebe, C. E., Pfister, H. & Lichtman, J. W. (2015). *Cell*, **162**, 648–661.
Kazuki, T., Shimpei, I. K., Takeru, Q. S., Etsuo, A. S., Dimitri, P., Maki, U., Hideki, U. & Hiroki, R. U. (2014). *Cell*, **159**, 911–924.
Kidoguchi, K., Tamaki, M., Mizobe, T., Koyama, J., Kondoh, T., Kohmura, E., Sakurai, T., Yokono, K. & Umetani, K. (2006). *Stroke*, **37**, 1856–1861.
Kobayashi, S., Hori, M., Dono, K., Nagano, H., Umeshita, K., Nakamori, S., Sakon, M., Osuga, K., Umetani, K., Murakami, T., Nakamura, H. & Monden, M. (2004). *J. Hepatol.* **40**, 405–408.
Krings, T. (2010). *Clin. Neuroradiol.* **20**, 5–24.
Kwanghun, C., Jenelle, W., Sung-Yon, K., Sandhiya, K., Aaron, S. A., Thomas, J. D., Julie, J. M., Kelly, A. Z., Joanna, M., Aleksandra, K. D., Sally, P., Hannah, B., Charu, R., Logan, G., Viviana, G. & Karl, D. (2013). *Struct. Mol. Interrogation Intact Biol. Syst. Nat.* **497**, 332–337.
Lang, S., Müller, B., Dominietto, M. D., Cattin, P. C., Zanette, I., Weitkamp, T. & Hieber, S. E. (2012). *Microvasc. Res.* **84**, 314–322.
Larrue, A., Rattner, A., Peter, Z. A., Olivier, C., Laroche, N., Vico, L. & Peyrin, F. (2011). *PLoS One*, **6**, e21297.
Lewis, R. (1997). *Phys. Med. Biol.* **42**, 1213–1243.
Li, A. A., Gong, H., Zhang, B., Wang, Q. D., Yan, C., Wu, J. P., Liu, Q. A., Zeng, S. Q. & Luo, Q. M. (2010). *Science*, **330**, 1404–1408.
Lin, H. M., Kou, B. Q., Li, X. T., Wang, Y. J., Ding, B., Shi, C., Liu, H. H., Tang, R. B., Sun, J. Q., Yan, F. H. & Zhang, H. (2015*a*). *PLoS One*, **10**, e0121438.
Lin, X., Miao, P., Mu, Z., Jiang, Z., Lu, Y., Guan, Y., Chen, X., Xiao, T., Wang, Y. & Yang, G. Y. (2015*b*). *Phys. Med. Biol.* **60**, 1655–1665.
Liu, P., Sun, J., Zhao, J., Liu, X., Gu, X., Li, J., Xiao, T. & Xu, L. X. (2010). *J. Synchrotron Rad.* **17**, 517–521.
Long, H. Q., Xie, W. H., Chen, W. L., Xie, W. L., Xu, J. H. & Hu, Y. (2014). *Int. J. Mol. Sci.* **15**, 12061–12073.
Longo, R. (2016). *Nucl. Instrum. Methods Phys. Res. A*, **809**, 13–22.
Lu, H., Wang, Y., He, X., Yuan, F., Lin, X., Xie, B., Tang, G., Huang, J., Tang, Y., Jin, K., Chen, S. & Yang, G. Y. (2012). *Stroke*, **43**, 838–843.
Lu, H. B., Zheng, C., Wang, Z. W., Chen, C., Chen, H. B. & Hu, J. Z. (2015). *PLoS One*, **10**, e0124724.
Lu, W. F., Dong, Z. H., Liu, Z. J., Fu, W. G., Peng, Y. F., Chen, S. L., Xiao, T. Q., Xie, H. L., Du, G. H., Deng, B. A. & Zhang, X. (2010). *J. Surg. Res.* **164**, e193–e199.
Lundström, U., Larsson, D. H., Burvall, A., Takman, P. A. C., Scott, L., Brismar, H. & Hertz, H. M. (2012). *Phys. Med. Biol.* **57**, 2603–2617.
Luo, Y. H., Yin, X. Z., Shi, S. P., Ren, X. L., Zhang, H. R., Wang, Z. L., Cao, Y., Tang, M. M., Xiao, B. & Zhang, M. Q. (2019). *Front. Neuroanat.* **13**, doi:10.3389/fnana.2019.00005.
Marín-Padilla, M. (2012). *Front. Neuroanat.* **6**, 38.
Martirosyan, N. L., Feuerstein, J. S., Theodore, N., Cavalcanti, D. D., Spetzler, R. F. & Preul, M. C. (2011). *J. Neurosurg. Spine*, **15**, 238–251.
Meuli, R., Hwu, Y., Je, J. H. & Margaritondo, G. (2004). *Eur. Radiol.* **14**, 1550–1560.
Momose, A., Takeda, T., Itai, Y. & Hirano, K. (1996). *Nat. Med.* **2**, 473–475.
Mori, H., Hyodo, K., Tanaka, E., Uddin-Mohammed, M., Yamakawa, A., Shinozaki, Y., Nakazawa, H., Tanaka, Y., Sekka, T., Iwata, Y., Handa, S., Umetani, K., Ueki, H., Yokoyama, T., Tanioka, K., Kubota, M., Hosaka, H., Ishikawa, N. & Ando, M. (1996). *Radiology*, **201**, 173–177.
Mori, H., Hyodo, K., Tobita, K., Chujo, M., Shinozaki, Y., Sugishita, Y. & Ando, M. (1994). *Circulation*, **89**, 863–871.
Mouchtouris, N., Jabbour, P. M., Starke, R. M., Hasan, D. M., Zanaty, M., Theofanis, T., Ding, D., Tjoumakaris, S. I., Dumont, A. S., Ghobrial, G. M., Kung, D., Rosenwasser, R. H. & Chalouhi, N. (2015). *J. Cereb. Blood Flow Metab.* **35**, 167–175.
Mu, Z. H., Jiang, Z., Lin, X. J., Wang, L. P., Xi, Y., Zhang, Z. J., Wang, Y. T. & Yang, G. Y. (2016). *CNS Neurosci. Ther.* **22**, 316–324.
Myojin, K., Taguchi, A., Umetani, K., Fukushima, K., Nishiura, N., Matsuyama, T., Kimura, H., Stern, D. M., Imai, Y. & Mori, H. (2007). *Am. J. Neuroradiol.* **28**, 953–957.
Pabst, A. M., Ackermann, M., Wagner, W., Haberthür, D., Ziebart, T. & Konerding, M. A. (2014). *J. Cranio-Maxillofac. Surg.* **42**, 915–923.
Peterzol, A., Bravin, A., Coan, P. & Elleaume, H. (2005). *Radiat. Prot. Dosim.* **117**, 44–49.
Pfeiffer, F., Bunk, O., David, C., Bech, M., Le Duc, G., Bravin, A. & Cloetens, P. (2007). *Phys. Med. Biol.* **52**, 6923–6930.
Pinzer, B. R., Cacquevel, M., Modregger, P., McDonald, S. A., Bensadoun, J. C., Thuering, T., Aebischer, P. & Stampanoni, M. (2012). *Neuroimage*, **61**, 1336–1346.
Qu, Q. M., Blom, H., Sanchez, S. & Ahlberg, P. (2015). *J. Morphol.* **276**, 873–888.
Rabin, O., Manuel Perez, J., Grimm, J., Wojtkiewicz, G. & Weissleder, R. (2006). *Nat. Mater.* **5**, 118–122.
Ragan, T., Kadiri, L. R., Venkataraju, K. U., Bahlmann, K., Sutin, J., Taranda, J., Arganda-Carreras, I., Kim, Y., Seung, H. S. & Osten, P. (2012). *Nat. Methods*, **9**, 255–258.
Raju, T., Li, Y., Brian, H. & Karl, D. (2014). *Nat. Protoc.* **9**, 1682–1697.
Risser, L., Plouraboué, F., Cloetens, P. & Fonta, C. (2009). *Int. J. Dev. Neurosci.* **27**, 185–196.
Risser, L., Plouraboué, F., Steyer, A., Cloetens, P., Le Duc, G. & Fonta, C. (2007). *J. Cereb. Blood Flow Metab.* **27**, 293–303.
Rubenstein, E., Hofstadter, R., Zeman, H. D., Thompson, A. C., Otis, J. N., Brown, G. S., Giacomini, J. C., Gordon, H. J., Kernoff, R. S. & Harrison, D. C. (1986). *Proc. Natl Acad. Sci. USA*, **83**, 9724–9728.
Schültke, E., Fiedler, S., Nemoz, C., Ogieglo, L., Kelly, M. E., Crawford, P., Esteve, F., Brochard, T., Renier, M., Requardt, H., Le Duc, G., Juurlink, B. & Meguro, K. (2010). *Eur. J. Radiol.* **73**, 677–681.
Schültke, E., Kelly, M. E., Nemoz, C., Fiedler, S., Ogieglo, L., Crawford, P., Paterson, J., Beavis, C., Esteve, F., Brochard, T., Renier, M., Requardt, H., Dallery, D., Le Duc, G. & Meguro, K. (2011). *Eur. J. Radiol.* **79**, 323–327.
Shirai, M., Schwenke, D. O., Eppel, G. A., Evans, R. G., Edgley, A. J., Tsuchimochi, H., Umetani, K. & Pearson, J. T. (2009). *Clin. Exp. Pharmacol. Physiol.* **36**, 107–116.
Shirai, M., Schwenke, D. O., Tsuchimochi, H., Umetani, K., Yagi, N. & Pearson, J. T. (2013). *Circ. Res.* **112**, 209–221.
Stevenson, A. W., Gureyev, T. E., Paganin, D., Wilkins, S. W., Weitkamp, T., Snigirev, A., Rau, C., Snigireva, I., Youn, H. S., Dolbnya, I. P., Yun, W., Lai, B., Garrett, R. F., Cookson, D. J., Hyodo, K. & Ando, M. (2003). *Nucl. Instrum. Methods Phys. Res. B*, **199**, 427–435.
Stolz, E., Yeniguen, M., Kreisel, M., Kampschulte, M., Doenges, S., Sedding, D., Ritman, E. L., Gerriets, T. & Langheinrich, A. C. (2011). *Neuroimage*, **54**, 1881–1886.
Suortti, P. & Thomlinson, W. (2003). *Phys. Med. Biol.* **48**, R1–R35.
Takashima, K., Hoshino, M., Uesugi, K., Yagi, N., Matsuda, S., Nakahira, A., Osumi, N., Kohzuki, M. & Onodera, H. (2015). *J. Synchrotron Rad.* **22**, 136–142.

Tang, R. B., Xi, Y., Chai, W. M., Wang, Y. T., Guan, Y. J., Yang, G. Y., Xie, H. L. & Chen, K. M. (2011). *Phys. Med. Biol.* **56**, 3503–3512.
Tapfer, A., Bech, M., Zanette, I., Symvoulidis, P., Stangl, S., Multhoff, G., Molls, M., Ntziachristos, V. & Pfeiffer, F. (2014). *J. Microsc.* **253**, 24–30.
Velroyen, A., Bech, M., Zanette, I., Schwarz, J., Rack, A., Tympner, C., Herrler, T., Staab-Weijnitz, C., Braunagel, M., Reiser, M., Bamberg, F., Pfeiffer, F. & Notohamiprodjo, M. (2014). *PLoS One*, **9**, e109562.
Wang, L. P., Mu, Z. H., Lin, X., Geng, J., Xiao, T. Q., Zhang, Z., Wang, Y., Guan, Y. & Yang, G.-Y. (2016). *Front. Aging Neurosci.* **9**, 359.
Xi, Y., Kou, B., Sun, H., Qi, J., Sun, J., Mohr, J., Börner, M., Zhao, J., Xu, L. X., Xiao, T. & Wang, Y. (2012). *J. Synchrotron Rad.* **19**, 821–826.
Xi, Y., Lin, X. J., Yuan, F. L., Yang, G. Y. & Zhao, J. (2015). *Comput. Math. Method. Med.* **2015**, 530580.
Yamashita, T., Kawashima, S., Ozaki, M., Namiki, M., Shinohara, M., Inoue, N., Hirata, K., Umetani, K. & Yokoyama, M. (2002). *Circ. J.* **66**, 1057–1059.
Yuan, F. L., Tang, Y. H., Lin, X. J., Xi, Y., Guan, Y. J., Xiao, T. Q., Chen, J., Zhang, Z. J., Yang, G. Y. & Wang, Y. T. (2012). *J. Neurotrauma*, **29**, 1499–1505.
Zernike, F. (1955). *Science*, **121**, 345–349.
Zhang, L., Hu, C. H., Zhao, T. & Luo, S. Q. (2011). *Eur. J. Radiol.* **80**, 158–162.
Zhang, M. Q., Peng, G. Y., Sun, D. N., Xie, Y. Y., Xia, J., Long, H. Y., Hu, K. & Xiao, B. (2014*b*). *Med. Phys.* **41**, 031907.
Zhang, M. Q., Sun, D. N., Xie, Y. Y., Peng, G. Y., Xia, J., Long, H. Y. & Xiao, B. (2014*a*). *Br. J. Radiol.* **87**, 20130670.
Zhang, M. Q., Zhou, L., Deng, Q. F., Xie, Y. Y., Xiao, T. Q., Cao, Y. Z., Zhang, J. W., Chen, X. M., Yin, X. Z. & Xiao, B. (2015). *Sci. Rep.* **5**, 14982.
Zhao, J. J., Lin, X. J., He, C., Yang, G. Y. & Ling, F. (2015). *J. Clin. Neurosci.* **22**, 373–377.
Zhao, Y., Brun, E., Coan, P., Huang, Z., Sztrókay, A., Diemoz, P. C., Liebhardt, S., Mittone, A., Gasilov, S., Miao, J. & Bravin, A. (2012). *Proc. Natl Acad. Sci. USA*, **109**, 18290–18294.
Zhu, P., Zhang, K., Wang, Z., Liu, Y., Liu, X., Wu, Z., McDonald, S. A., Marone, F. & Stampanoni, M. (2010). *Proc. Natl Acad. Sci. USA*, **107**, 13576–13581.